Maximum a posteriori estimation of crystallographic phases in X-ray diffraction tomography

Doğa Gürsoy[1], Tekin Biçer[2], Jonathan D. Almer[1],
Rajkumar Kettimuthu[2], Stuart R. Stock[3], Francesco De Carlo[1]

[1]X-ray Science Division, Advanced Photon Source,
Argonne National Laboratory
[2]Mathematics and Computer Science Division,
Argonne National Laboratory
[3]Department of Cell and Molecular Biology,
Feinberg School of Medicine, Northwestern University

February 11, 2015

Submitted to: Phil. Trans. R. Soc. A

Abstract

A maximum a posteriori (MAP) approach is proposed for X-ray diffraction tomography for reconstructing three-dimensional spatial distribution of crystallographic phases and orientations of polycrystalline materials. The approach maximizes the posterior density which includes a Poisson log-likelihood and a prior term that reenforces expected solution properties such as smoothness or local continuity. The reconstruction method is validated with experimental data acquired from a section of the spinous process of a porcine vertebra collected at the 1-ID-C beamline in the Advanced Photon Source, at Argonne National Laboratory. The preliminary results show significant improvement on reduction of streaking artifacts, and robustness to noise and undersampling than the conventional analytical inversion approaches. The approach has the potential to reduce data acquisition times, and significantly improve beamtime efficiency.

1 Introduction

X-ray powder diffraction is a routine analytical tool for characterization of materials, and when combined with tomography, it becomes a powerful technique for studying three-dimensional (3D) spatial distribution of crystallographic phases and orientations of polycrystalline materials [**?**]. When a monochromatic X-ray beam irradiates a specimen containing a multitude of single crystals which have various orientations, the diffraction pattern consists of concentric Debye cones from the different crystallographic planes, characterized by the index triplet *hkl*, the so-called Miller indices [**?**]. For a narrow, pencil-shaped incident X-ray beam, and an area detector positioned normal to the beam, the cones intersect the detector plane as a series of concentric rings whose opening angles, i.e., diffraction angles $2\theta_{hkl}$ depend on X-ray wavelength λ, and inter-planar spacing d_{hkl} (and lattice parameters) through Bragg's law: $\lambda = 2d_{hkl}\sin\theta_{hkl}$ [**?**]. In X-ray diffraction tomography (XDT), the pencil beam is translated across the specimen, producing a "projection" image data, and the process is repeated for the projection angles required for reconstruction. Often a scalar, additive quantity is required for each raster scan location as an input to the reconstruction algorithms, and the conventional approach is to integrate the diffraction rings radially, converting the 2D diffraction patterns into 1D radial diffraction patterns. Each 2θ bin then produces a separate reconstruction $I_{2\theta}(x, y)$ of the sample's cross-section, where I is the intensity of the volume element or voxel at position x, y within the slice. Then, for a single x, y one can combine I from the different 2θ reconstructions to produce a 1D diffraction pattern for that voxel.

Analytical methods like filtered back projection (FBP) [**?**] has been the traditional method of choice for reconstructing the 3D crystallographic phases within the specimen. While FBP provides fairly quick and robust results, the reconstruction quality is severely affected with increasing undersampling and noise. Statistical approaches, on the other hand, often provides better quality images, because they allow for incorporating better models of

the imaging physics, and also allows for utilizing prior information about possible solutions when the data is incomplete [**?**]. This provides a great flexibility in inverse modeling for dealing with sub-optimal data acquisition schemes. Many similar problems are formulated by modeling a cost function corresponding to a probability distribution over model parameters, and the goal is to obtain the maximum a posteriori (MAP) model estimates that are consistent with existing data and prior assumption about the solutions [**?**]. In this paper, a similar approach is proposed for X-ray diffraction tomography for reconstructing 3D spatial distribution of crystallographic phases and orientations of polycrystalline materials. The approach maximizes the posteriori density which includes a Poisson log-likelihood and a prior term that reenforces expected solution properties such as smoothness or local continuity. The reconstruction method is validated with experimental data acquired from a section of the spinous process of a porcine vertebra to image the spatial crystalline orientations in the sample. The advantage of this approach is that prior knowledge such as smoothness or roughness can be imposed on the reconstructed diffraction patterns, which in turn improves the accuracy of the reconstructed phases.

Similar to other statistical iterative algorithms, the proposed method also demands significant computational resources in order to obtain reconstructions within a reasonable time. Each iteration requires solution of the forward problem, which calculates the Radon integrals along each beam path for a given diffraction angle. This process is a highly compute-intensive task and needs efficient parallel algorithms and high-end computing systems. We implemented our reconstruction algorithms on a high-performance data-intensive computing middleware [**?**] and performed image reconstruction at Argonne Leadership Computing Facility. Specifically, we ran our experiments on Mira, a 10-petaflops IBM Blue Gene/Q system. We used up to 1200 nodes where each node consists of 16 physical cores (19200 cores in total) and 16GiB memory. The execution time of 3D reconstruction takes only about 240 milliseconds per single MAP iteration, which indicates that the reconstruction

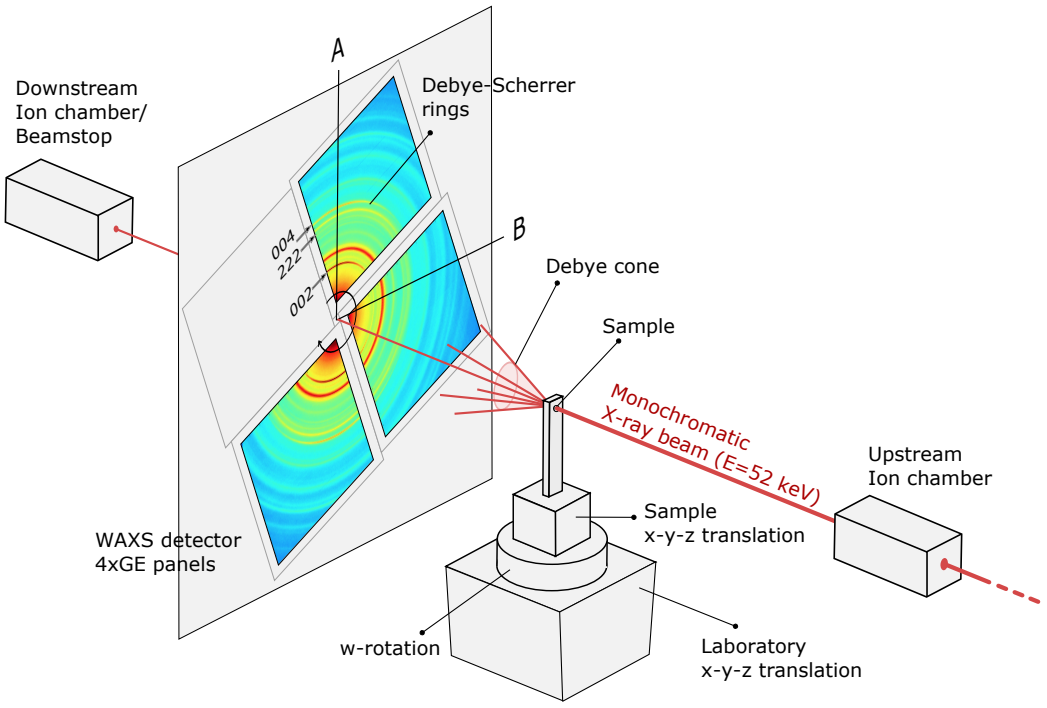

Figure 1: Schematic illustration of synchrotron instrumentation at the 1-ID-C beamline in the Advanced Photon Source, at Argonne National Laboratory. High-energy X-rays incident on the sample are forward-scattered into Debye cones, which are measured with four GE detectors. The sample is translated along B-axis and rotated in w to provide diffraction-tomography data. Transmission data is collected simultaneously with ion-chambers before and after the sample.

can be performed near-real time. The following sections describe the performed diffraction experiment, and the individual data processing steps to obtain the final crystalline phases of the material.

2 Materials and methods

2.1 Measurement setup

XDT measurements were acquired from a spinous process of a porcine vertebra acquired at the 1-ID-C beamline in the Advanced Photon Source, at Argonne National Laboratory,

using an X-ray energy of 52 keV formed by an undulator and brilliance-preserving monochromator (see, Figure **??** for schematic illustration). The X-ray beam was horizontally defined by slits along B-axis, and vertically focused along A-axis using refractive lenses to provide a beam size of 25×50 (A-B) μm at the sample location. Diffraction data was recorded using four GE RT-41 panels, arranged as shown in Figure **??** to collect different portions of Debye rings, nominally perpendicular to the direct beam, and at a sample-detector distance of 2165 mm. The detectors were calibrated (tilt/beam center) using a National Institute of Standards and Technology (NIST) ceria standard. To collect a XDT dataset for a given layer (A-position), detector images were taken at 1 second intervals, over 184 degrees in w at 2 degree steps ($N_w = 93$). The sample was then translated 200 μm along B-axis and this process repeated for a total of 110 positions ($N_B = 110$) to cover the entire sample cross-section, for a total collection time of about 3 hours per layer. Multiple layers ($N_A = 5$) were recorded, here we focus on results from a single layer.

2.2 Data preprocessing

The recorded intensity maps at a particular beam position are shown in Figure **??**. At first, the input data are transformed from polar to Cartesian coordinates to perform radial integration over the highlighted triangular regions around the vertical and horizontal directions. The radial positions are then transformed to d-spacings using geometric parameters given in the previous section. Often the powder diffraction curve follows a smooth trajectory along the radial direction, consisting of Bragg peaks resting on a smooth background. This can be mathematically expressed by,

$$I = \sum_p I_p + I_b. \tag{1}$$

According to this expression, the measured intensity I has both a contribution from the background signal I_b, and each of the Bragg reflections I_p near peak locations. Note that the

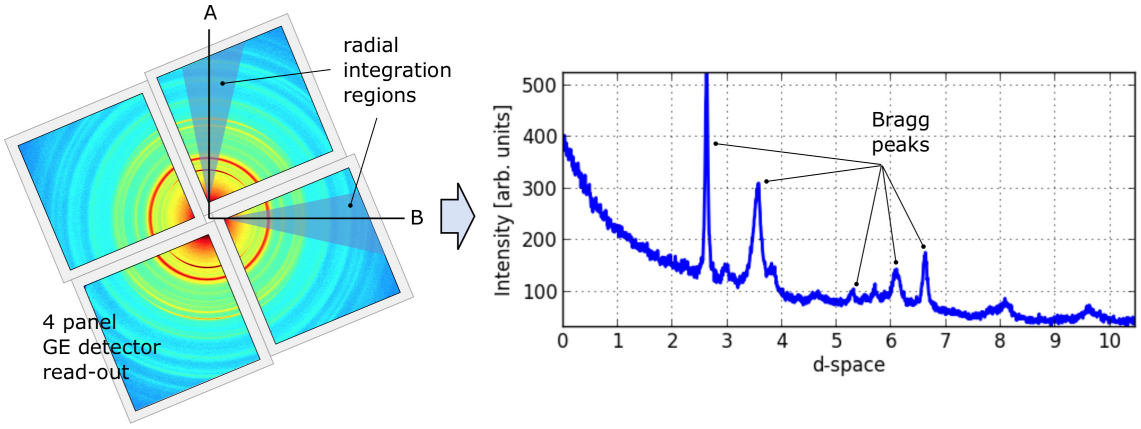

Figure 2: Powder diffraction measurement that was recorded using four GE RT-41 panels at a particular beam position is shown on the left. A radial integration is performed along the highlighted vertical (A-axis) and horizontal (B-axis) directions to obtain the corresponding 1D diffraction patterns at each beam position. Often this pattern follows a smooth trajectory along the radial direction, consisting of Bragg peaks resting on a smooth background.

background signals are considered as statistically independent from the crystalline diffraction processes. This allows for a straightforward background subtraction over a specified range as follows,

$$I_{ij}^{'} = I_{ij} - \frac{1}{2e+2}\left(\sum_{j=0}^{e} I_{ij} + \sum_{j=r-e}^{r} I_{ij}\right), \quad i = 1, \ldots, \eta \tag{2}$$

where r and η are the total number of pixels in radius and azimuth axes, respectively, and the term in brackets is the background. The scalar e determines the number of boundary pixels on each side of the radial image to be used for calculation of the background, and usually selected a few pixels in size. In this expression, we assume the approximation, $I^{'} \approx \sum_p I_p$ holds, which is generally a valid argument assuming slow variations in background intensity. These $I_{ij}^{'}$ values, i.e., the background corrected intensity distributions for each diffraction, are then used for tomographic image reconstruction as described in the next section.

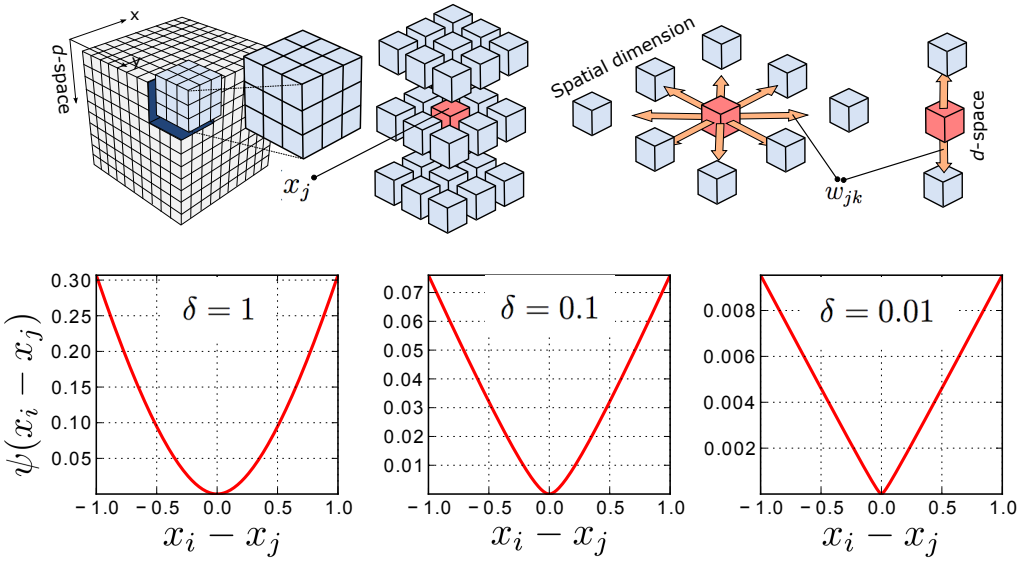

Figure 3: A three-dimensional "data cube" (with 2D spatial and 1D d-space variations), and the interactions among neighboring voxels in spatial coordinates and d-spacings are illustrated at the top. The regularization function for various δ values are plotted at the bottom.

2.3 Image reconstruction

This section describes the process of reconstructing the crystalline phases for each point in the sample from the background corrected diffraction data. We formulate the problem in a MAP framework by combining the data likelihood and prior terms, which leads to a discrete optimization problem in the general form of [**?**]:

$$x_{MAP} = \arg\max_{x \geq 0} \{\mathcal{L}(x, y) - \beta \mathcal{R}(x)\}, \tag{3}$$

where x_{MAP} is the so-called MAP estimate. $x \in \mathbb{R}^N$ and $y \in \mathbb{R}^M$ are respectively the discrete model and data parameters. The objective function consists of a Poisson log-likelihood $\mathcal{L}(x, y)$ and prior terms $\mathcal{R}(x)$ to regularize variations among the local neighborhood of the model parameters. The regularization parameter β is to control the trade-off between the data likelihood and the prior terms. The MAP estimator formulated in this way can also be

interpreted as a penalized maximum likelihood estimator [**?**]. With this approach, instead of directly maximizing the data-likelihood [**?**], a number of prior terms can be used to reenforce desired (e.g. smoothness, sharpness) and/or certain (e.g. non-negativity) properties of the solution [**?**]. A common form of a prior term is [**?**]:

$$\mathcal{R}(x) = \sum_i \sum_{j \in N} w_{ij} \psi(x_i - x_j), \tag{4}$$

where $\psi(.)$ is a user-defined functional with dependency only on the difference values of model parameters in a set of voxels (N) in a neighborhood of the ith voxel, that is, eight neighboring voxels in the spatial cross-section, and two voxels in the neighboring d-spacings (see, Figure **??** for a visual illustration of the prior model). The constants w_{ij} are nonnegative weights that satisfy w_{ij}=w_{ji} for all i and j. The weights are normally set inversely proportional to the Euclidean distance between the neighboring voxels. Often, $\psi(x)$ is selected from monotonically nondecreasing functions of quadratic forms, that is, $(x_i - x_j)^2$, which leads to smooth images while greatly reducing the likelihood of sharp transitions of the model parameter across adjacent voxels. Non-quadratic forms can as well be used, particularly to favor preservation of sharp boundaries. In this paper, we used the following function [**?**]:

$$\psi(x) = \delta^2 \left[\left| \frac{x}{\delta} \right| - \log \left(1 + \left| \frac{x}{\delta} \right| \right) \right], \tag{5}$$

which provides smooth solutions for large δ values, however favors piecewise-constant structures for finite values of δ, thus, allowing either a quadratic or a quasi-linear model to describe parameter variations. A natural choice for the solution is to use larger δ values to impose smoothness in the diffraction domain (i.e., d-space) and to use smaller δ for the spatial domain. A closed form expression for the solution of the optimization problem was obtained using the optimization transfer principle [**?**].

2.4 Image analysis

After the diffraction data are fully reconstructed, an identification procedure is applied along the radial axis to determine individual crystalline phases. Typically, a region-of-interest (ROI) analysis by summing the values along a given azimuthal range is sufficient to localize known phases. The following expression describes the process:

$$x_i^K = \frac{1}{\Delta r}\sum_{j=r_s}^{r_f} x_{ij} - \frac{1}{2(e+1)}\left(\sum_{j=r_s-e}^{r_s} x_{ij} + \sum_{j=r_f}^{r_f+e} x_{ij}\right), \quad i = 1, \ldots, \eta \tag{6}$$

where K is used for indexing the phases, x_i is the reconstructed scalar value of a given pixel, r_s and r_f are the starting and ending radii of a given ROI, with Δr as the corresponding difference. Similar to the background subtraction in the preprocessing phase, the second term in the brackets is the contribution from a slowly changing background, and e is used to determine the number of boundary pixels on each side of the radial image. The final phase reconstructions associated with various ROIs can be constructed by forming an image by assembling the x_i values in a 2D image matrix in spatial cross-section of the specimen.

3 Results

We initially performed radial integrations in the vertical and horizontal directions on image data to obtain individual 1D diffraction patterns for every beam scan position (as previously described in Figure **??**). We then removed the background from diffraction data using equation (**??**) with $e = 3$. This provided a 3D projection data (2D for the spatial dimensions, and 1D for the d-space) as input to the reconstruction algorithm. The voxel sizes for the corresponding input data were 200 μm and 5 millidegrees in spatial and diffraction dimensions, respectively. MAP reconstructions are obtained after 200 iterations, and the results are presented in Figure **??**. The resolutions of model and data parameters were

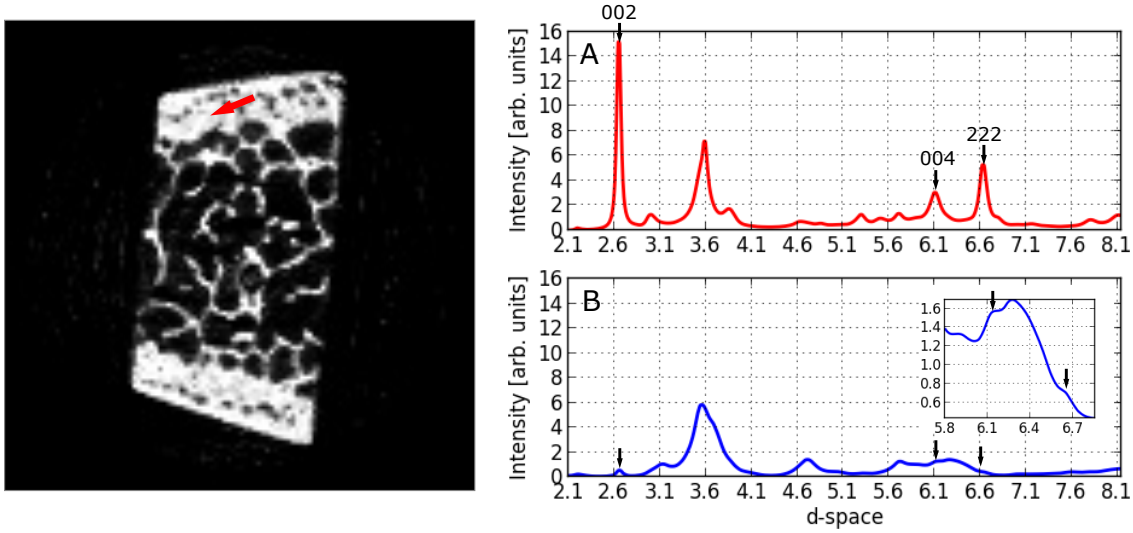

Figure 4: The image on the left corresponds to the reconstruction of the cross-section at $2\theta = 3.59$ degrees. The plots on the right are the reconstructed diffraction patterns at a particular voxel pointed with the red arrow on the left image. The reconstructed Bragg peaks for $hkl = 002$, 004, and 222 are highlighted with arrows on the plots.

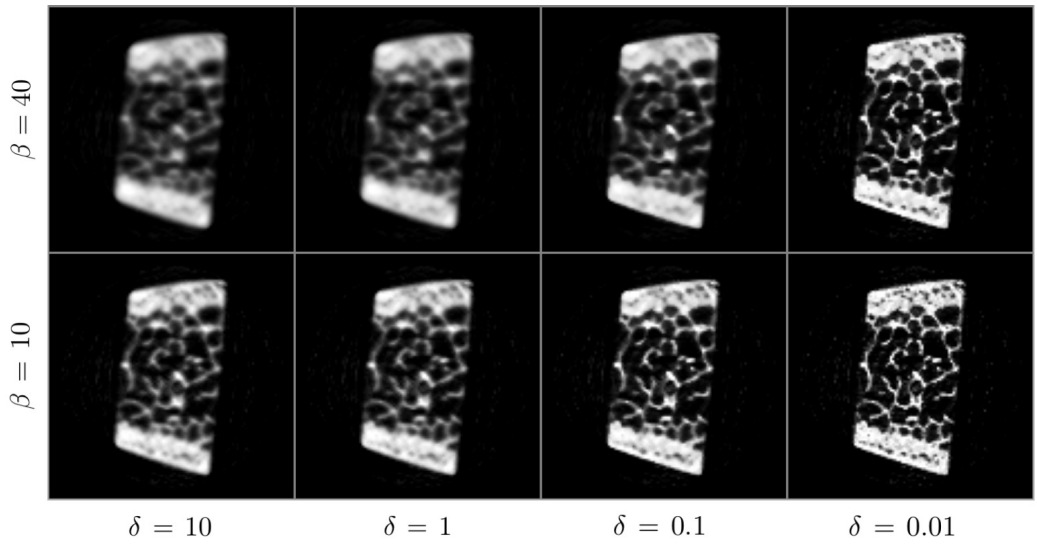

Figure 5: Demonstration of the effect of algorithm parameters (i.e., β and δ) on reconstructed images after 200 iterations.

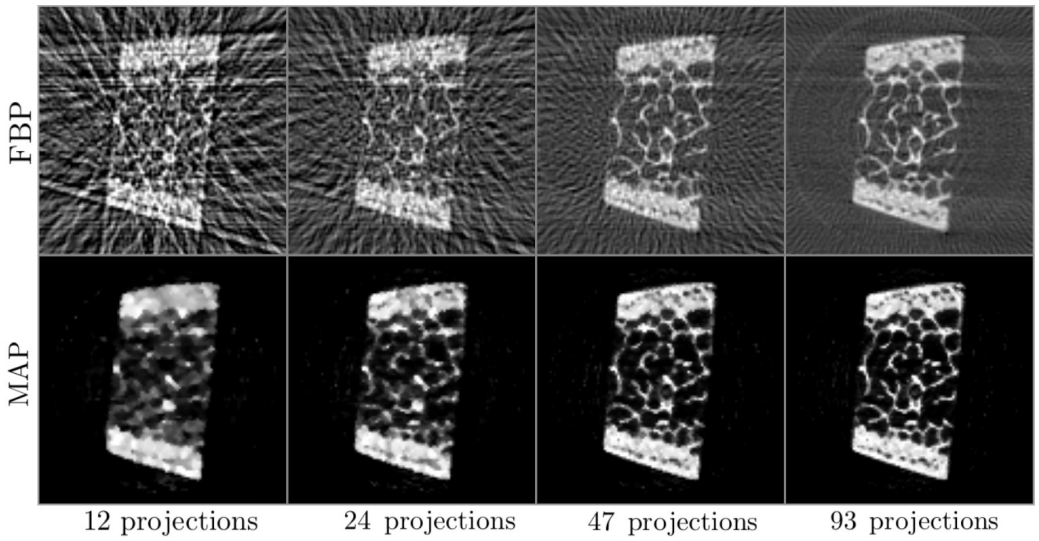

Figure 6: Comparison of MAP reconstruction with filtered back-projection for different undersampling ratios.

$93 \times 1200 \times 110$ $[projections \times d-spacings \times raster-locations]$ and $155 \times 155 \times 1200$, respectively. The cross-section image corresponds to the reconstruction at $2\theta = 3.59$ degrees on vertical axis. The red and blue curves respectively corresponds to the reconstructed vertical and horizontal diffraction patterns at a particular voxel within the specimen highlighted with red arrow. The plots clearly demonstrate the differences between diffraction patterns along vertical (A) and horizontal (B) directions, particularly at the Bragg peaks of hkl = 002, 004, and 222. Figure **??** shows the effect of algorithm parameters (i.e., β and δ) on reconstructed images. Larger δ values leads to smoother images, whereas using smaller δ values provides sharp and clear images. With increased regularization, i.e., for larger β values, the corresponding effect is amplified. Figure **??** shows the comparison of MAP estimation with the conventionally used filtered back-projection (FBP) method for different undersampling or data compression ratios. We used the regridding algorithm for FBP implementation, where the interpolations are carried out in the Fourier domain rather than in spatial domain [**?**]. Streaking artifacts are clearly visible in images obtained with

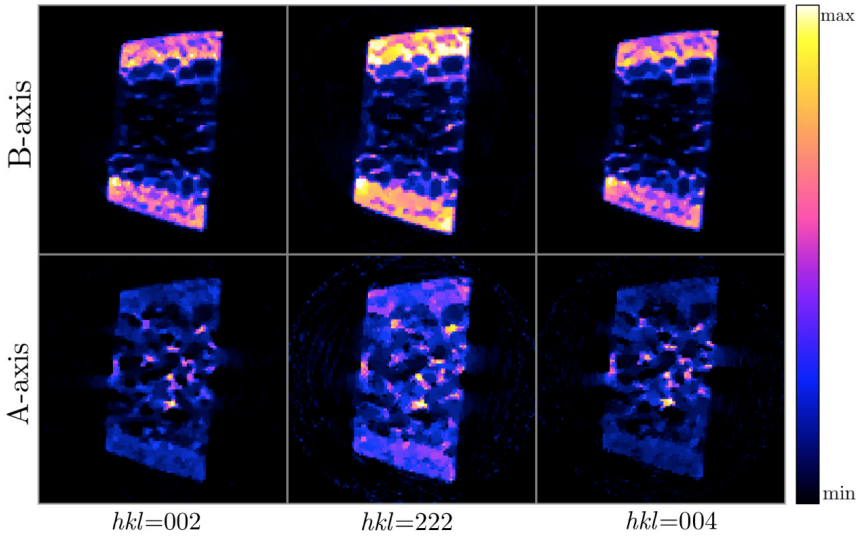

Figure 7: Reconstructed crystallographic phases for hkl = 002, 004, and 222 from the integrated areas of the associated Bragg peaks. The top and bottom rows correspond to the phases obtained by integrating the corresponding Bragg peaks within the reconstructions for the vertical and horizontal diffraction directions. The external cortex is present on opposite sides of the specimen and is where muscles attach. The interior of the specimen contains trabeculae which brace the cortex. The cortical and trabecular bone experience very different loading states *in vivo* and are expected to possess very different carbonated hydroxyapatite (cAp) preferred orientations.

FBP, even when using the complete dataset with 93 projections. MAP reconstruction removed these artifacts, while preserving a remarkable image sharpness. Reducing data sizes by 2 and 4 times did not produce significant quality degradation in MAP reconstruction, and maintained good image quality even with data having as low as 24 projections. Figure **??** shows the crystallographic phases for hkl = 002, 004, and 222 that were obtained by integrating the corresponding Bragg peaks according to equation **??**. The external cortex is present on opposite sides of the specimen and is where muscles attach. The interior of the specimen contains trabeculae which brace the cortex. The cortical and trabecular bone experience very different loading states *in vivo* and are expected to possess very different carbonated hydroxyapatite (cAp) preferred orientations, i.e., $hkl = 002, 222$.

4 Discussions

Absorption-based reconstructions are widely used in bone studies and have added greatly to understanding of degraded bone structures in maladies as diverse as osteoporosis and osteolytic lesions in bone metastases. As discussed above, XDT of bone offers information very different from that of absorption tomography, not just where the bone mass is present but how that mineral is organized. Preferred orientation of mineral (nanoplatelets of carbonated hydroxyapatite, cAp) within bone, for example, greatly affects functionality and is an important input for numerical models. One could section the specimen and quantify mineral orientation vs. position via a raster scan, but that would not allow repeated non-invasive interrogation of the sample as it was loaded. The specimen is of interest from a biomineralization standpoint, as it exhibits considerable heterogeneity including crystallographic texture, but also from the perspective of developing XDT.

On challenge in inverse modeling of X-ray tomographic data is that the samples may come in various shapes, features, and properties. This necessitates having a wider range of priors, or constraints, that must individually be set according to the sample type for optimal results. The proposed MAP approach for X-ray tomography allows the necessary flexibility for defining priors on general model properties like smoothness, edginess, non-negativity, etc., and also the inclusion of other non-trivial prior distributions by training to further reveal the subtle local statistics about the sample (e.g. porosity, crack propagation, fluid diffusion, etc.). Currently, we are exploring ways for classifying high-dimensional X-ray datasets and samples, not only for the case of XDT, but also for other tomography techniques like X-ray fluorescence tomography [**?**], and time-resolved micro-CT [**?**].

Smart tomographic systems with integrated software (i.e. reconstruction algorithm) and data acquisition hardware are of particular interest, which allows for optimizing experiments while data is being collected. XDT is particularly suitable for such *in situ* and *in transit* data analysis, because the data acquisition is typically slow due to the raster scanning of the

sample with a pencil beam. An integrated approach is when MAP iterations are launched using a subset of data while data is being collected, and advancing iterations with newly added data will progressively reduce the uncertainty of the reconstructions. This kind of combined data acquisition and analysis allows many new possibilities for optimal design of experiments, and improving the efficiency of experiments.

5 Conclusions

In this paper, we introduced a MAP approach for X-ray diffraction tomography to perform 3D reconstruction of crystallographic phases and orientations of polycrystalline materials. This multidimensional inversion approach allows provides the capability to yield the full diffraction spectrum for each spatial voxel in the sample, and avoids conventional reconstruction artifacts. We tested the reconstruction method with experimental diffraction data acquired from a bone sample. The preliminary results show significant improvement on reduction of streaking artifacts, and robustness to noise and undersampling than the conventional analytical inversion approaches.

6 Acknowledgements

This research used resources of the Advanced Photon Source, a U.S. Department of Energy (DOE) Office of Science User Facility operated for the DOE Office of Science by Argonne National Laboratory under Contract No. DE-AC02-06CH11357. Stuart R. Stock acknowledges support from NICDR grant DE001374.

References

[1] Abbey B, Hofmann F, Belnoue J, Rack A, Tucoulou R, Hughes G, Eve S, Korsunsky AM. 2011. Mapping the dislocation sub-structure of deformed polycrystalline Ni by

scanning microbeam diffraction topography. *Scr. Mater.* **64**.

[2] Cullity BD, Stock SR. 2001. *Elements of X-ray diffraction*. New Jersey, USA: Prentice Hall.

[3] Dinnebier RE, Billinge SJL. (ed.) 2008. *Powder diffraction: Theory and practice*. Cambridge, UK: RSC Publishing.

[4] Kak AC, Slaney M. 2001. *Principles of computerized tomographic imaging*. Philadelphia, PA: SIAM.

[5] Kaipo J, Somersalo E. 2004. *Statistical and computational inverse problems*. New York, NY: Springer.

[6] Bicer T. 2014. Supporting data-intensive scientific computing on bandwidth and space constrained environments. *PhD Dissertation*.

[7] Hansen PC. 2010. *Discrete inverse problems: Insight and algorithms*. Philadelphia, PA: SIAM.

[8] Tarantola A.2004. *Inverse problem theory and methods for model parameter estimation*. Philadelphia, PA: SIAM.

[9] De Pierro A. 1995. A modified expectation maximization algorithm for penalized likelihood estimation in emission tomography. *IEEE T. Med. Imaging* **14**.

[10] Shepp LA, Vardi Y. 1982. Maximum likelihood reconstruction for emission tomography. *IEEE T. Med. Imaging* **1**.

[11] Qi J, Leahy RM. 2006. Iterative reconstruction techniques in emission computed tomography. *Phys. Med. Biol.* **51**.

[12] Moussouris J. 2014. Gibbs and Markov random systems with constraints. *J. Stat. Phys.* **10**.

[13] Lange K. 1990. Convergence of EM image reconstruction algorithms with Gibbs smoothing. *IEEE T. Med. Imaging* **9**.

[14] Chang JH, Anderson JMM, Votaw JR. 2004. Regularized image reconstruction algorithms for positron emission tomography. *IEEE T. Med. Imaging* **23**.

[15] Dowd B. A., Campbell G. H., Marr R. B., Nagarkar V., Tipnis S., Axe L., Siddons D. P. 1999. Developments in synchrotron x-ray computed microtomography at the National Synchrotron Light Source. *Proc. SPIE,* **3772**, 224–236.

[16] Gürsoy D, De Carlo F, Xiao X, Jacobsen C. 2014. TomoPy: A framework for the analysis of synchrotron tomographic data. *J. Synchrotron Radiat.* **21**.

[17] Gürsoy D, Lanzirotti A, Newville MG, De Carlo F. Hyperspectral image reconstruction for X-ray fluorescence tomography. *(in revision).*

[18] Duke DJ, Swantek AB, Sovis N, Tilocco FZ, Gürsoy D, Powell CF. 2015. Time-resolved X-ray tomography of gasoline direct injection sprays. *JSAE/SAE Powertrains, Fuels and Lubricants International Meeting.*